International Journal of Biological Macromolecules 204 (2022) 333–344

Contents lists available at ScienceDirect

International Journal of Biological Macromolecules

journal homepage: www.elsevier.com/locate/ijbiomac

Lignin grafted hydroxyapatite entrapped in polyacrylamide: Characterization and adsorptive features for Th^{4+} and bovine serum albumin

Fuat Aslan [a,1], Demet Baybaş [b], Ulvi Ulusoy [a,*]

[a] Sivas Cumhuriyet University, Science Faculty, Chemistry Department, Sivas 58140, Turkey
[b] Sivas Cumhuriyet University, Science Faculty, Biochemistry Department, Sivas 58140, Turkey

ARTICLE INFO

Keywords:
Hydroxyapatite
Lignin
Polyacrylamide
Thorium
BSA
Adsorption

ABSTRACT

Water-soluble sulfolignin (SL) was grafted onto hydroxyapatite (Hap) by using epichlorohydrin. SLgHap was then entrapped in cross-linked polyacrylamide by in situ polymerizations of acrylamide and *N*, *N*′-methylenebisacrylamide to obtain the composite of PSLgHap. The composite was characterized by FT-IR, BET- porosity, XRD, EDXRF, SEM-EDX, TGA-DTG, PZC, CEC, and swelling tests. The adsorptive features of PSLgHAP were investigated for Th^{4+} and BSA in view of its dependence on pH, ionic intensity, concentration, temperature, and time. The results of characterization tests confirmed the formation of PSLgHap. The grafting efficiency concerning sulfur contents of PSLgHap was 96% by EDXRF. The isotherms were best represented by the Sips model, Langmuir adsorption capacities were 369 and 390 mg g_{SLgHap}^{-1} for BSA and Th^{4+}. The enthalpy and entropy changes were positive whilst Gibbs energy was negative by entropy controlled. The adsorption kinetics of both species was obeyed to pseudo second-order model, whereas it was first-order for BSA and hybrid-order for Th^{4+} of Langmuir model.

1. Introduction

Environmental protection is of the major concerns for a sustainable quality of life. Indeed, alongside the rapid development of industrialization on a global scale, the entry of industrial effluents with inorganic, organic, and biological pollutants into the water resources of modern society has become a serious environmental issue. Therefore, a large variety of treatment technologies for the removal/recovery of contaminants from the polluted aquatic environment and waste streams have been invented and developed. These technologies include adsorption, ion exchange, precipitation, coagulation-flocculation, sedimentation, flotation, filtration, membrane processes, biological processes, and chemical reactions. Amongst these, adsorption is one of the most commonly used methods due to its number of advantages, e.g., simple operation process, high efficiency, good adaptability for different wastewater systems, and particularly low cost [1–3].

The principal concern of this study is to introduce a new composite adsorbent with a ternary combination of lignin, hydroxyapatite, and polyacrylamide. Lignin was chosen since it is also a nature-derived highly abundant biopolymer alongside cellulose and hemicellulose. Annual lignin production as a by-product of the pulp and paper industries is about 50 million tons. Of this, only one million tons are processed for various industrial products, almost the rest is used as boiler fuel for heat and electricity generation or directly discharged into water resources [4,5]. Lignin-based materials are immensely important in the industry with their wide range of applications, e.g., stimulant-sensitive materials for biomedical and water treatment, drug delivery systems [6,7], flexible super-capacitors, wearable electronics, biomaterials, particle dispersants in the formulation of coatings, adhesives, and composites [8–11]. Recently, Wang et al. [12] investigated the antibacterial activity via the electrostatic capture effect of silver nanoparticles incorporated quaternized lignin composites synthesized by the aid of microwave radiation. Lignin is biocompatible and biodegradable. Because of its unique physicochemical features, low cost, high abundance, and the containment of specific functional groups on its macromolecular structure, lignin has been considered as an adsorbent for the removal of organic or inorganic contaminants from the aquatic environment [8,13,14].

* Corresponding author.
E-mail addresses: faslan@erbakan.edu.tr (F. Aslan), dbaybas@cumhuriyet.edu.tr (D. Baybaş), ulusoy@cumhuriyet.edu.tr (U. Ulusoy).
[1] Present address: Necmettin Erbakan University, Science and Technology Research and Application Center (BİTAM), Konya 42140, Turkey.

https://doi.org/10.1016/j.ijbiomac.2022.01.200
Received 23 November 2021; Received in revised form 21 January 2022; Accepted 31 January 2022
Available online 4 February 2022

Hydroxyapatite (Hap) as the other composite component is the best-known crystal phase of calcium phosphate salts defined by the $Ca_{10}(PO_4)_6(OH)_2$ general formula. Hap as a Ca—P based bioceramics, is a biocompatible, bioactive, and osteoconductive material since its Ca/P ratio is close to the ratio in natural bone and tooth structure, and is the most stable calcium phosphate under physiological conditions. Hap possesses a multi-site binding character for proteins; the C region rich in Ca ions with the positive charge is attractive for the acidic terminals whereas the positive charge deficient P region attracts the basic terminals. Based on this feature, the sintered Hap (mechanically strengthened with high heat treatment) has been widely employed as supporting material in column applications as in HPLC for protein adsorption and protein separation, and cellular attachment and growth. Besides these, its participations in orthopedic, and dental materials, drug release systems, and protein carriers are of a variety of applications [15–18]. It is also promising material for the elimination of air, water, and soil pollution due to its features such as high adsorption capacity, inexpensive and readily available, acid-base adjustability, ion exchange capability, low water solubility, good thermal stability, and high stability under reducing-oxidizing conditions. Since its stability and leak-resistance, Hap is also a favorable material for the permeable reactive barriers used for remediation of areas contaminated with radionuclide and safely manage long-life nuclear waste by storing it in deep geological deposits [19].

The Hap compositions are useful materials for the adsorption procedures. However, the physicochemical features of Hap limit its practical utilization in column applications because of the column blockage. The use of Hap-polymer composites should be a solution to overcome this handicap. The polymer component should have swelling in aquatic solutions capability enabling the diffusion and/or transfer of the ions towards the mineral. Indeed, the practical applicability of this opinion was proved for Hap-cellulose for Pb^{2+}, Cu^{2+}, Cd^{2+}, Zn^{2+} adsorption [20], Hap-polyurethane composite for lead ion uptake [21], Hap-Poly (vinyl alcohol) composite cryogel for cadmium removal [22], and for polyacrylamide-Hap (PAAm-Hap) composite for recovery of Pb^{2+} [23], and UO_2^{2+} and Th^{4+} ions [24]. The synthesis and mechanical properties of nano-Hap/PAAm composite were reported by Li et al. [25].

As implemented of PAAm in the Hap practicality, grafting of lignin, especially sulfolignin which is not usable in adsorption practices due to its solubility in the aquatic environment, onto a polymer network could also enable its practical usage as previously proved for kraft lignin by Meister et al. [26]. Peñaranda et al. [27] proposed to use of IPN hydrogels involving peat and kraft lignin for adsorption of Ni^{2+} and Cu^{2+} ions. For the production of the lignin-containing marketable plastics, acrylamide was grafted onto organosolv lignin by the chemo-enzymatic method [28]. Chen et al. [29] introduced PAAm/Lignin nanocomposite hydrogels with high mechanical strength, excellent recoverability as well as high compressive and tensile strength. Synthesis of the composite was simple (in situ free radical polymerization), it was non-cytotoxic so that this high-performance hydrogel material could be used in e.g. tissue engineering or regeneration, artificial muscles, underwater antifouling materials. In another study, the self-assembly of kraft lignin-acrylamide polymers in aqueous solutions containing different amounts of salt was evaluated [30]. The synthesis of bio-composite in a combination with Lignin and Hap was proposed by Erakovic et al. [31] where Ag containing Hap and Lignin biocomposite coatings on titanium were produced by the electrophoretic deposition method and characterized, and its antimicrobial properties were investigated.

In consequence, none of the aforementioned studies has considered the composite composed of a ternary combination of water-soluble Sulfolignin (SL), as the grafting component, Hap, and PAAm; PSLgHap. The confinement in PAAm prevents possible coagulation/agglomeration of SLgHap in the adsorption medium where it is used in its bare form. Since the sulfur sources are SL and Hap, the grafting efficiency can be precisely determined by the comparison of sulfur contents of SL, Hap, and PSLgHap. The employment of XRF for sulfur determination will be a highly practical technique. Synthesis of such composite improves the adsorptive feature of SLgHap due to its fine dispersion in PAAm hydrogel increasing surface expansion; the composite is swollen in adsorbates solution during which the adsorbates transfer towards the finely dispersed adsorptive centers, i.e., the adsorption process is ultimately catalyzed. The purpose of this investigation was to introduce the preparation and characterization of the PSLgHap and to investigate its adsorptive features for thorium (Th^{4+}) and bovine serum albumin (BSA). The choice of Th^{4+} was due to the environmental concerns associated with toxicity and radioactivity besides which the recovery of Th^{4+} from natural sources and/or nuclear waste may be of economic interest [32]. To investigate the adsorptive properties for BSA was also prominent since BSA is one of the major serum proteins having a vitally important role in functional, and nutritional activities, and functional similarity to human serum albumin [33,34]. Its low cost, wide availability, and high affinity to Hap made the BSA adsorption worthy of perusing besides that such investigation could be an introduction of a new adsorbent for protein purification process, and contribution to the establishment of the nature of interactions between adsorptive surface and proteins [35].

2. Experimental

2.1. Chemicals

Sulfonated lignin [Lignosulfonic acid, sodium salt; REAX 85A; $\{(CH_3O)NaO)Ar(CH_2SO_3Na)_x(C_3H_6O)\}_y$] kindly provided by Mead-Westvaco Corp. (USA). The phosphate rock (hydroxyapatite; Hap) supplied by Samsun Fertilizer Laboratories (Turkey) was utilized in the preparation of PSLgHap after ground and sieved in 100 mesh size. The composition of the rock was 46.4% of CaO, 24.9% of P_2O_5, 9.3% of SiO_2, 1.6% of SO_3, 0.5% of Fe_2O_3, 1.6% of MgO, and the metal oxides at trace levels. The stoichiometric coefficient of n_{Ca}/n_P is ≈1.67 in both pure phosphate rock $[Ca_5(PO_4)_3(OH)_{0.33}F_{0.33}Cl_{0.33}]$ and Hap in the form of bio-origin $[Ca_{10}(PO_4)_6(OH)_2]$ [36]. However, the ratio values for naturally occurring differ from this value as reported by Mavropoulos et al. [37] for 5 phosphate mining sites as 2.22 ± 0.32 (ranging 2.06–2.77). Here, the ratio for the studied Hap was 2.37 confirming its natural origin.

Bovine serum albumin (BSA), coomassie brilliant blue G-250, sodium nitroprusside, and *N*, *N*′-methylbisacrylamide (Sigma, USA), phenol, Th $(NO)_3.4H_2O$, acrylamide monomer, ammonium peroxydisulfate, HCl, glacial CH_3COOH, HNO_3, KBr, and KNO_3 (Merck, Germany), *N*, *N*, *N*′, *N*′-Tetramethylethylenediamine (TEMED), Arsenazo III [2,7-Bis(2-arsonophenylazo)-1,8-dihydroxy naphthalene-3,6-disulfonic acid disodium salt], epichlorohydrin (ECH) (Fluka-Sigma, USA) $Al(NO_3)_3.9H_2O$, $Pb(NO_3)_2$, $CuCl_2.2H_2O$, $ZnCl_2$, $Cr(NO_3)_3.9H_2O$, $MnSO_4.H_2O$, $NiCl_2.6H_2O$ and $CoCl_2.6H_2O$ (Merck, Germany), solution of $NaClO_4$ with %15 active chlorine content were the chemicals, all were analytical grade, and used without any further purification. The resistivity of distilled water was 18 MΩ cm^{-1} at room temperature.

2.2. Preparation of PSLgHAP composite

The procedure provided by Dragan et al. [38] was modified to prepare the Lignin-Hap (LH) component of PSLgHap. In obtaining 8 g of PSLgHap, 1 g of Hap was suspended in a 25 mL viscous solution containing 3% of acetic acid and 1 g of sulfolignin preconditioned by intense stirring for 4 h. After the addition of 25 mL of ECH solution in water (v_{ECH}/v_{H2O} = 1/20 at pH = 10), the mixture was agitated for an additional 4 h. Under intense and continuous stirring, 6 g of AAm and 20 mL of *N*, *N*′-methylbisacrylamide solution (0.03 g mL^{-1}) as the crosslinking agent of PAAm were added to the suspension respectively. While the suspension was stirred to keep homogeneity, the polymerization was started by the addition of 1 mL ammonium peroxydisulfate (100 mg

mL^{-1}) solution as initiator and 0.5 mL of *N*, *N*, *N′*,*N′*-tetramethylenediamine as an activator. The formed PSLgHap, the composite in which lignin grafted Hap was entrapped in a hydrogel network was immediately dispersed in 250 mL of water by passing the composite throughout a syringe system (barrel and plunger). The dispersion was waited for about 1 h with slight stirrings and the aqueous phase was decanted, the washing and decantation procedure was repeated to remove unreacted chemicals. The composite was spread out of Petri-dishes and dried in an oven at 40 °C, ground, and sieved to <50 mesh.

2.3. Characterization

FT-IR spectra were taken using an FT-IR spectrophotometer (Unicam, Mattson 1000) with 20 scans at a resolution of 4 cm^{-1}. Rigaku Ultima-IV was employed for XRD patterns (2Θ = 3-70°) at 0.02° scan interval using Cu K_α radiation. EDXRF (Rigaku – NEX – CG) was utilized for the determination of the elemental composition of PSLgHap and its associates. Nitrogen adsorption/desorption isotherms were performed at 77 K with AUTOSORB-6 (Quantachrome Instruments) apparatus. BET and BJH methods were used to obtain the specific surface area, pore diameters, and volumes. SEM and EDX views of gold-coated samples were obtained from QUANTA 400F Field Emission SEM with an accelerating voltage of 20 kV. TGA curves were obtained for the mass losses at temperatures within the range of 20–900 °C at 10 °C min^{-1} heating rate under static air with Perkin Elmer Pyris 1.

Swelling kinetics was investigated. 0.3 g of PSLgHap sample was let to swell in water and weighed at time intervals.

Univalent cation exchange capacities (CEC) of the composite and its components were determined by the ammonium acetate method [39].

The point of zero charges (pH_{PZC}) of the composite and its associates was measured in presence of 0.1 M KNO_3 as an inert electrolyte [40]. 0.1 g of samples were suspended in 10 mL of KNO_3 solutions with adjusted initial pHs (pH_i) ranging from 1 to 12 by using 0.1 M of KOH or HNO_3. The equilibrium pHs (pH_e) were measured after 24 h solid solution interaction.

2.4. Adsorptive features for Th^{4+} and BSA

The dependence of Th^{4+} and BSA adsorption on PSLgHap to pH, concentration, time (kinetics), temperature (thermodynamic), and ionic intensity were examined.

An Arsenazo III (Az-III)-Th^{4+} complex formation based spectrophotometric procedure was followed for Th^{4+} measurements [41]; 50 μL of equilibrium solution transferred in 3 mL of complexation solution containing %0.04 Az-III in 3 M $HClO_4$. Absorbency of the formed complex at 658 nm was recorded (Shimadzu-160A spectrophotometer), the pure Az-III solution was the reference.

Bradford method was employed for colorimetric measurement of BSA for which a prescription modified from a bio-protocol by He [42] was preferred. A 50 μL fraction of BSA solution was added to 2.5 mL of Coomassie Brilliant Blue G–250 and the absorbance at 595 nm was recorded, Bradford reagent was the reference solution. Linear standard calibration curves obtained from the absorbency of BSA or Th^{4+} solutions were used to determine equilibrium concentrations obtained from the experiments.

Initial pHs of solutions in the pH effect on adsorption studies were in the ranges of 1–10 for BSA and 1–7 for Th^{4+} adjusted by the addition of HCl or NaOH. After the evaluation of the pH effect on the adsorption, all adsorption studies were performed at initial pH = 3 for BSA and pH about 3.5 for Th^{4+} as prepared. With exception of the kinetics studies, the interaction time for equilibrium was 24 h, as a convention. Out of the thermodynamic study, all experiments were carried out at 298 K. Effect of the concentration change on BSA or Th^{4+} adsorption was studied for the range of 25–2000 ppm (3.8×10^{-7}-3×10^{-5} M or 1.1×10^{-4}-8.6×10^{-3} M). The studied concentration was constant at 1000 ppm (1.5×10^{-5} M or 4.3×10^{-3} M) in all other adsorption tests.

Table 1
Physical characteristics of PSLgHap and its constituents.

	BET/m^2g^{-1}	Pore Volume x10^3/cm^3g^{-1}	Pore radius/nm
SL	8.2	11.3	3.0
Hap	24.1	94.8	3.8
PAAm	11.5	9.3	3.7
PSLgHap	6.6	6.3	2.1

The adsorption kinetics was examined by time interval sampling (50 μL) from the test solution during 24 h adsorbent-solution interaction.

Ionic intensity impact on the adsorption was performed for BSA or Th^{4+} solution in 0.01–025 M $CaCl_2$.

3. Results and discussion

3.1. Characterization

3.1.1. Porosity, surface charge, and cation exchange capacity

The size of pore diameters of the ter-composite and its constituents were in the range of 2–4 nm (Table 1) defining the nano/meso-porous structure according to the IUPAC classification [43]. The BET and pore volume of PSLgHap was considerably lower than that of Hap. This was associated with the filling of PAAm into the mineral pores as seen from the morphologic comparisons of SL, Hap, and PSLgHap in Fig. 1. The EDX spectra of Th adsorbed PSLgHap in Fig. 1.d displayed the elements identifying PAAm (C, N, and O), SL (Na, S), and Hap (Ca, P).

The PZC (point of zero charge) is the pH at which the surface of a solid adsorbent immersed in an electrolyte has zero charges referring to the surface charge switches from positive at pH < PZC and to negative at pH > PZC. The data obtained from PZC experiments provided PZC values and buffering features of the materials calculated from the linear equations derived from ΔpH (pHe-pHi) vs pH_i and the buffering pH range obtained from the plateau region of pH_e vs pH_i (Fig. 2). The PZC of PSLgHap was 7.6 as nearly identical to its buffering pH. PAAm had the PZC at pH = 6.5 and did not have the buffering feature. The CEC values of Hap and PSLgHap were 0.47 and 2.83 mol NH_4^+/kg. The significant difference in the CEC in favor of PSLgHap was due to the increase in active sorption sites, after SL and ECH involvement in SLgHap formation. The CEC of PAAm was negligible (CEC < 0.01 mol NH_4^+/kg).

Consequently, the changes in CEC values besides which the BET and porosity feature substantiated that the encapsulation of Hap, i.e., SLgHap in an inert hydrogel (PAAm) resulted in a formation of a new structure having physiochemical features completely different from its associates.

3.1.2. EDXRF, FT-IR, and XRD analysis

EDXRF was utilized for the determination of the grafting efficiency by tracing elemental sulfur contents of SL, Hap, and PSLgHap out of PAAm since it does not contain any sulfur. The contents of sulfur as the means of 3 measurements having the standard deviations statistically insignificant ($p < 0.05$) were 5.29% for SL, 0.65% for Hap, and 0.71% for PSLgHap. Since the sulfur contribution to PSLgHap from SL and Hap was 12.5% for each, the theoretical sulfur content of PSLgHap was expected to be 0.74% ($5.29 \times 0.125 + 0.65 \times 0.125$). Thus, the grafting efficiency was found to be 95.9% ($100 \times 0.71/0.74$). This result should also be valid for the experimental PSLgHap formation efficiency because Hap always remained as a dispersed solid phase without any loss during the synthesis process.

FT-IR spectra of Hap, SL, and PAAm were compared with that of its PSLgHap combination in Fig. 3. For Hap, the intensive peaks at 560 and 600 cm^{-1} and 1000–1100 cm^{-1} were of PO_4^{3-} groups. The stretches associated with CO_3^{2-} were characterized by the intense bands at 1450–1550 cm^{-1}. Broadband at 3000–3600 cm^{-1} should be related to -OH of adsorbed water to Hap [44].

As pointed out by Nair et al. and Rashid et al. [45,46] typical

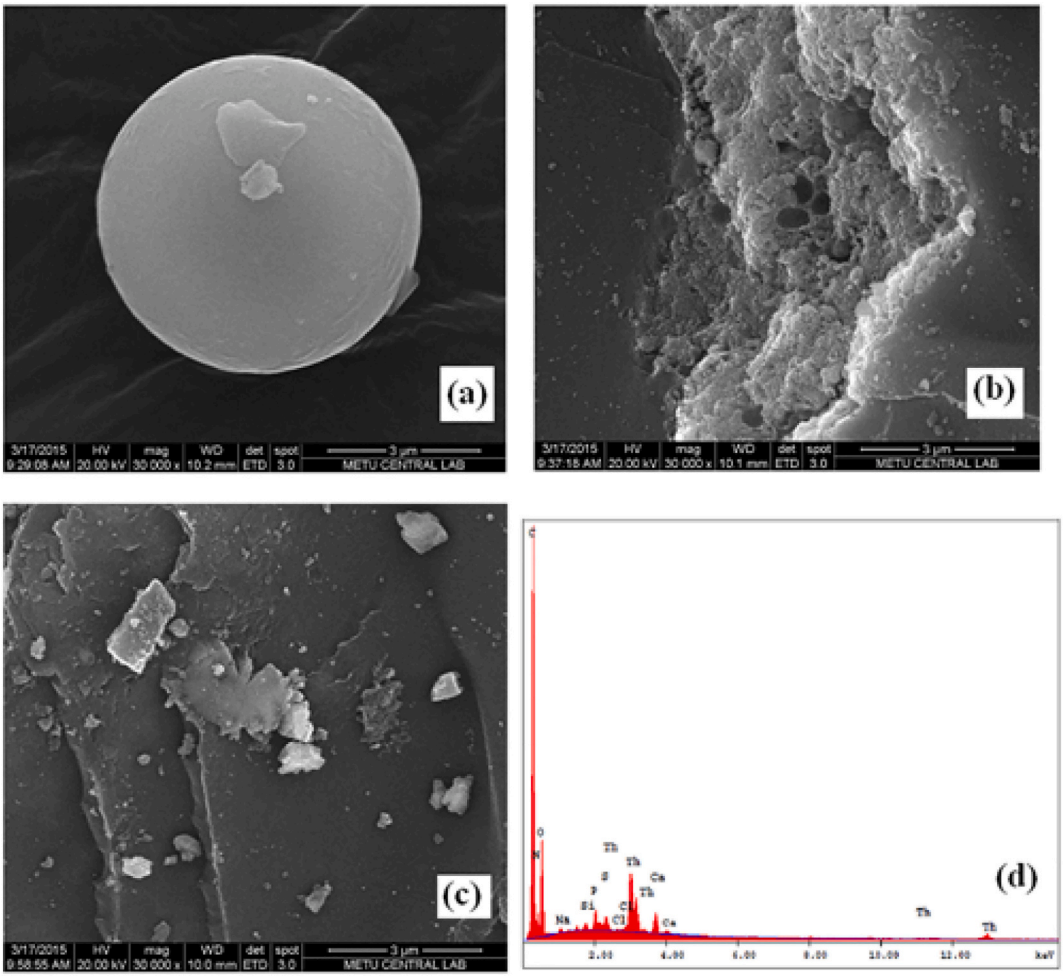

Fig. 1. SEM appearance of SL (a) with a spheriform view of an SL particle, Hap (b) likens to agglomerations of mineral grains and PSLgHap (c) in an appearance of amorphous layers in the combination of PAAm, SL and Hap, and EDX spectra of PSLgHap after Th adsorption (d).

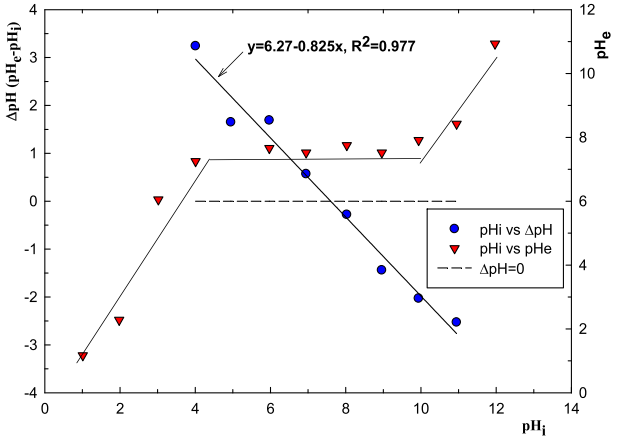

Fig. 2. The PZC and buffering determinations by pH studies.

appearances in SL's IR spectra were broadband at 3460–3350 cm^{-1} for aliphatic and/or aromatic –OH, the peaks at around 2940 and 2830 cm^{-1} attributable to C—H bonds in aromatic and alkyl groups, and the peaks at around 1600 and 1520 cm^{-1} associated with C=C stretches of the phenolic groups. Besides these, the skeletal vibrations in the wavenumbers ranging from 1600 cm^{-1} to 1000 cm^{-1} were typical definitions for the aromatic units of lignin structure.

PAAm was characterized by the peaks associated with C—N (1192 cm^{-1}), C—C (1323 cm^{-1}), -CH_2 (1452 cm^{-1}), -$CONH_2$ (1670 cm^{-1}), C—H in –$CONH_2$ (1570 and 1720 cm^{-1}), and N—H in -$CONH_2$ (3185 and 3450 cm^{-1}) [47,48]. The spectra of PSLgHap demonstrated that the composite was the combination of Hap, SL, and PAAm for which the appearances at 560–1100 cm^{-1} representing PO_4^{3-} groups of Hap, several peaks in between 1600 and 1000 cm^{-1} associated with aromatic components of SL, and the typical peaks emerging at 3185–3450 cm^{-1}, 1570–1720 cm^{-1} ranges characterizing -$CONH_2$ related terminals were of evidence.

Fig. 4 shows the XRD patterns of PSLgHap together with its associates. The patterns of bare SL and PAAm defined typical noncrystalline (amorphous) structures. The hexagonal structure of Hap was consistent with the 2θ diffractions at 26° (L002), 32° (L211), 33° (L300), and 40° (L310). The patterns of Hap and PSLgHap were confirmed that the confinement of the Hap in PAAm did not disrupt the crystalline structure of Hap. The increased background in the patterns of composites was due to the irregular reflections arising from the amorphous structure of PAAm and SL [24,49,50].

3.1.3. *Thermal stability*

The results obtained from the TGA and DTG analysis of the materials were submitted in Fig. 5 and Table 2.

Hap had three-stage weight losses at 25–200 °C, 200–600 °C, and 600–900 °C. The loss in a total of 2.6% at 25–600 °C was associated with the evaporation of adsorbed and lattice water confirming the high thermal stability of Hap by 600 °C. The considerable loss (16.6%) over

Fig. 3. FT-IR spectra of SL, Hap, PAAm and PSLgHap.

700 °C was due to the removal of water formed from the dehydroxylation of Hap as discussed by Tonsuaadu et al. (2012) [51]. The removal of moisture in PAAm was also completed by 200 °C. The characteristic peaks in PAAm were related to the emissions of H_2O, CO_2, and NH_3 after decomposition of amide groups at 200–350 °C, the losses of H_2O, CO_2, imides and nitriles after the main chain breakdown at 350–450 °C, and the releases during carbonization of the polymer at 450–600 °C [47]. Since SL had a wide variety of functional groups such as aromatic, carbonyl, and hydroxyl besides the sulfonyl groups, thermal degradation of SL had a mass loss profile that covers the whole range of temperature change. The degradations correlated with the decarboxylation and desulfurization reactions [52], and the formation of volatile CO and/or CO_2 after oxidation of carbon contents of SL [53]. As expected, the thermal degradation profile of PSLgHap was very similar to that of the PAAm since the PAAm content of PSLgHap was about75%. A slight rise at $t_{1/2}$ (from 395 °C for PAAm to 408 °C for PSLgHap) was attributable to SL in PSLgHap with $t_{1/2} = 816$ °C.

3.1.4. Swelling features

The swelling features of the composite were tested to propose the kinetics and mechanism of swelling because of its importance in the practical implementation in biomedicine, pharmacy, and environment. Swelling characteristics of the composite and its associates were

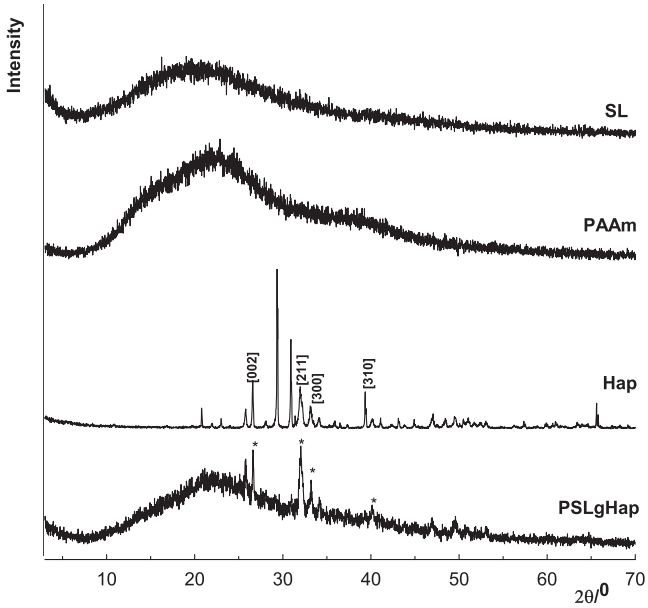

Fig. 4. XRD patterns of the composite and its components (The reflections labeled with asterisks characterized Hap in PSLgHap).

provided as water absorption capacity (S_e), Swelling%, and water contents at equilibrium (S_{WCE}) in Table 3.

PSLgHap had high water absorbency because of its constituents' contribution to the imbibing capacity. The measured parameters for the composite were higher than the calculated ones by considering the contribution of the feature of each constituent as much as its fraction in the composite. This should be evidence for the formation of a new synergetic texture with the inclusion of SL having chemical end groups with high water affinity.

The parameters associated with the kinetics were derived from the compatibility of data to the linear forms of Schott's second-order [$t/S_t = 1/(k_s S_m^2) + t/S_m$] and linearized exponential heuristic [$\ln(S_t/S_m) = \ln(F) + n.\ln(t)$] equations (Fig. 6) where 'S_t 'and S_m are the amount of adsorbed water at time 't (min)' and the amount reached a maximum ($g_{H2O}\ g_{PSLGHAP}{}^{-1}$), k_s is the Schott's rate constant ($g_{PSLgHAP}\ g_{H2O}{}^{-1}\ min^{-1}$), $1/(k_s S_m^2)$ is also defined as inverse initial adsorption rate ($1/r_0$). 'F' is a constant characterizing the hydrogel network and 'n' is diffusion constant peculiar to water transfer/swelling mechanism; the process controlled by solvent diffusion (Fickian) if $n < 0.5$, by solvent diffusion, and the relaxation of hydrogel network (non-Fickian) if '$0.5 < n < 1'$ or by relaxation of hydrogel if '$n > 1'$ [54,55]. The exponential model was evaluated by considering the data up to which 70% of the swelling was completed.

The results (Table 4) showed that the experimentally obtained swelling data were well compatible with both Schott and Fick models with high significance ($R^2 > 0.97$). The compatibility to Schott's model was persistent with an agreement between the values of S_{exp} ($8.2\ g_{H2O}.g_{PSLgHAP}{}^{-1}$) in Table 4 and S_m ($8.2\ g_{H2O}.g_{PSLgHAP}{}^{-1}$) in Table 5. Consequently, as indicated in previous reports the driving force for the water diffusion was osmotic pressure and the mechanism was Fickian ($n < 0.50$), i.e., the process was diffusion controlled [54,56]. It was worth noting that the value of the initial water imbibing rate was remarkably high ($29.3\ g_{H2O}\ g_{PSLgHAP}{}^{-1}\ min^{-1}$).

3.2. Adsorptive features of PSLgHap for BSA and Th^{4+} adsorption

3.2.1. Data assessment

The nomenclature and units used in the equations were as follows (Table 5).

The adsorbed amounts of Th^{4+} was calculated by using Eq. (1).

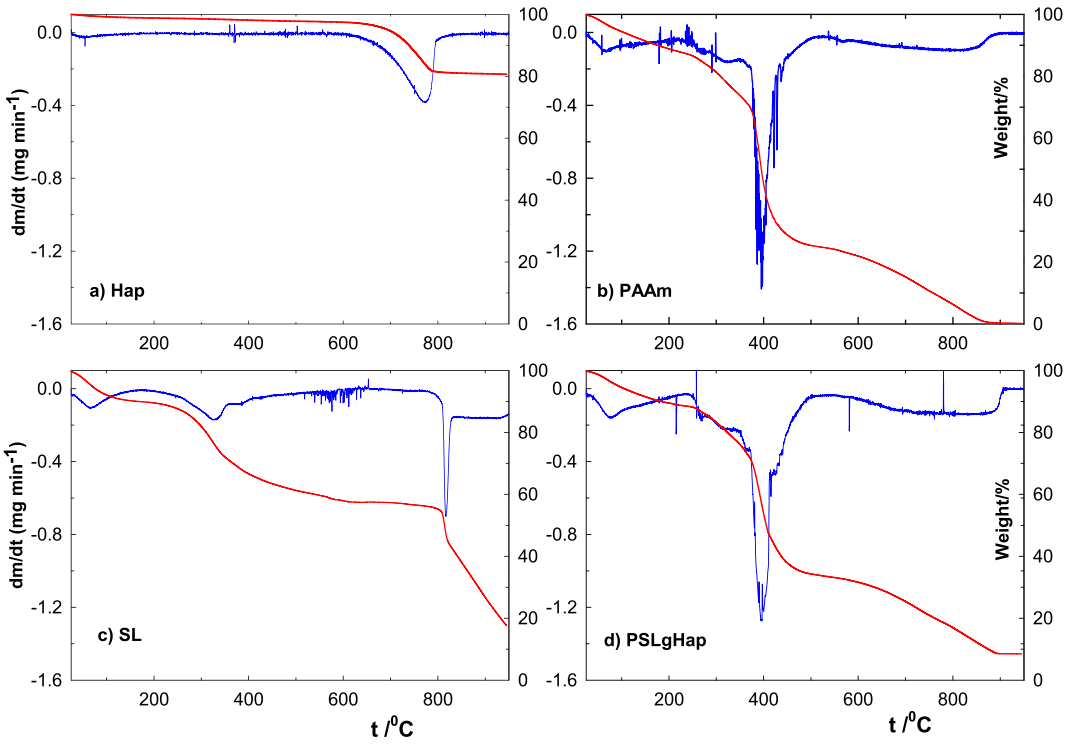

Fig. 5. TG (t vs weight%) and DTG patterns of PSLgHap and its associates.

Table 2
Percentage weight loss of the composite and its components between various temperature ranges (the summed provided the total lost between 25 and 900 °C).

	25–200 °C	200–600 °C	600–900 °C	25–900 °C	[b]$t_{1/2}$ °C
Hap	1.2 (54)[a]	1.4	16.6	19.2	–
PAAm	11.0 (58)	66.9 (270, 395)	21.6	99.5	395
SL	14.4 (65)	31.8 (325, 576)	31.1 (817)	77.3	816
PSLgHap	10.3 (80)	57.9 (215,394, 581)	23.1	91.3	408

[a] Characteristic DTG peaks at which the maximum lost was observed.
[b] Temperature by which half of the weight was lost.

Table 3
Swelling characteristics of the composite and its associates [Water absorption capacity, $S_e = (m_{max}\text{-}m_0)/m_0$; Swelling% = $(m_{max}x100/m_0)$ and water contents at equilibrium $S_{WCE}\% = (m_{max}\text{-}m_0)x100/m_{max}$ with reference to weights of dry and swollen materials; m_0 and m_{max}].

Materials	S_e (g_{H2O}/g_{mat})	Swelling/ %	S_{WCE} /%
Hap	1.6	260	61
PAAm	8.1	910	89
PSLgHap (75% PAAm, 12.5% Hap, 12.5% SL)[a]	8.2 (6.3)[b]	916 (720)[b]	89 (74)[b]

[a] Constituent contents of the composite (SL is water soluble).
[b] The expected values calculated by taking into account of Hap and PAAm contribution, e.g., 0.125 × 260 + 0.75 × 910 = 720%.

$$Q = \frac{(C_i - C_e)V}{W} \quad (1)$$

Adsorption parameters were derived from the compatibility of experimentally obtained adsorption isotherms to Langmuir, Freundlich, Sips, and Dubinin-Radushkevich (DR) models expressed by the following equations [57].

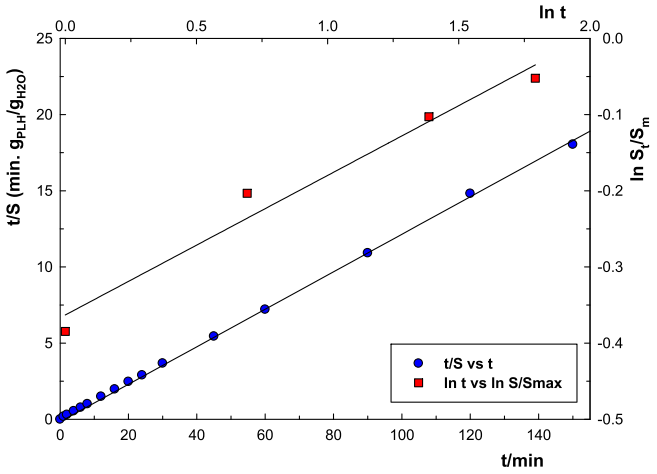

Fig. 6. Compatibility of swelling kinetics of PSLgHap to Schott's second-order and linearized exponential models.

Table 4
Parameters obtained from swelling kinetics for PSLgHap.

Schott's Model		Fick Model	
$k_s x10^3/g_{H2O}\ g^{-1}g\ min^{-1}$	0.43	F	0.70
$S_m/g_{H2O}\ g_{PSLgHAP}{}^{-1}$	8.3 (8.2)[a]	n	0.18
R^2	0.999	R^2	0.971
$r_0/g_{H2O}\ g_{PSLgHAP}{}^{-1}\ min^{-1}$	29.3		

[a] Experimentally obtained values of water absorption at equilibrium.

Table 5
Nomenclature and units for the data processing.

a_S: Sips isotherm model constant	$t_{1/2}$: Time required for adsorption of half of the concentration/min
$C_{i,\ e}$: BSA or Th^{4+} concentrations at initial or equilibrium/ mol L^{-1}	V: Solution volume/L
D: Adsorbent dose (kg L^{-1})	W: Mass of adsorbent/kg
E_{DR}: Free energy change/J mol^{-1}	X_{DR}: DR constant related to sorption capacity
H: Initial adsorption rate/mol^{-1} kg min^{-1}	X_F: Freundlich constant related to sorption capacity
k: Rate constant	X_L: Langmuir monolayer sorption capacity/mol kg^{-1}
K_{DR}: Constant in DR model/mol^2 K J^{-2}	X_S: Sips monolayer sorption capacity/ mol kg^{-1}
K_L: Langmuir adsorption equilibrium constant/L mol^{-1}	β: Freundlich constant (surface heterogeneity)
K_s: Sips isotherm model constant	$β_S$: Sips isotherm model exponent
Q: Adsorbed amounts/mol kg^{-1} at time t or equilibrium	ΔG: Change in adsorption free energy/ kJ mol^{-1}
R: Ideal gas constant (8.314 J mol^{-1} K^{-1})	ΔH: Change in adsorption enthalpy/kJ mol^{-1}
T: Absolute temperature/K	ΔS: Change in adsorption entropy/J mol^{-1} K^{-1}
	ε: Polanyi potential
	Θe: Surface coverage ratio

$$Q = \frac{K_L X_L C_e}{1 + K_L C_e} \quad \text{Langmuir} \tag{2}$$

$$Q = X_F C_e^{\ \beta} \quad \text{Freundlich} \tag{3}$$

$$Q = \frac{X_s a_s C_e^{\ \beta s}}{1 + a_s C_e^{\ \beta s}} \quad \text{Sips} \tag{4}$$

$$Q = X_{DR} e^{-K_{DR}\varepsilon^2} \quad \varepsilon = RTln\left(1 + \frac{1}{C_e}\right) \quad \text{DR} \tag{5}$$

$$E_{DR} = (-2K_{DR})^{\frac{1}{2}} \quad \text{DR} \tag{6}$$

Thermodynamics parameters were ascertained from the values of distribution coefficients (K) at studied temperatures. By the depictions of 'ln K vs 1/T' to configure the van t'Hoff equation provided magnitude of ΔH and ΔS followed by ΔG.

$$K = \frac{Q}{C_e} \tag{7}$$

$$lnK = \frac{\Delta S}{R} - \frac{\Delta H}{R}\frac{1}{T} \tag{8}$$

$$\Delta G = \Delta H - T\Delta S \tag{9}$$

The kinetics of Th^{4+} adsorption was inspected by the compatibility of time-dependent adsorption to pseudo first- and second-order, and intraparticle diffusion models (Eqs. (10)–(12)). The obtained parameters for first- and second-order models were forwarded to calculate the initial adsorption rate (H) and the time elapsed to reach half of the Th^{4+} adsorption at equilibrium; half-life ($t_{1/2}$) [58,59].

$$Q_t = Q_{e1}\left(1 - e^{-k_1 t}\right) \quad H_1 = k_1 Q_{e1} \quad \left(t_{1/2}\right)_1 = \frac{ln2}{k_1} \tag{10}$$

$$Q_t = \frac{Q_{e2}^2 k_2 t}{1 + Q_{e2} k_2 t} \quad H_2 = k_2 Q_{e2}^2 \quad \left(t_{1/2}\right)_2 = \frac{1}{k_2 Q_{e2}} \tag{11}$$

$$Q_t = k_i t^{1/2} \tag{12}$$

The order of kinetics was evaluated further by using the following equations to calculate the experimental and theoretical filling ratio of adsorptive sites, and the ratio of first and second-order rate constants derived from the Langmuir model [60];

$$(\Theta_e)_{\exp} = \frac{C_i - C_e}{X_L D} \tag{13}$$

$$(\Theta_e)_{theor} = \frac{K_L(C_i + X_L D) + 1 - \sqrt{K_L^2(C_i - X_L D)^2 + 2K_L(C_i + X_L D) + 1}}{2K_L X_L D} \tag{14}$$

$$\frac{k_1}{k_2} = \frac{\sqrt{K_L^2(C_i - X_L D)^2 + 2K_L(C_i + X_L D) + 1}}{K_L X_L D} \tag{15}$$

3.2.2. Adsorption dependence on pH and ionic intensity

The adsorption dependency of BSA as a function of pH at initial and equilibrium and the ionic strength was displayed in Fig. 7. The pHs at which a material has nil electrical charge, i.e., the number of sites negatively and positively charged on its surface are equal were pH = 7.6 (PZC) for PSLgHap and pH = 4.7 (the isoelectric point; pI). The dominant charge on the surface is positive at pH < PZC or pI, and it is negative at pH < PZC or pI. As illustrated in Fig. 7.a, BSA adsorption initially increased with increasing pH and reached a maximal at $pH_i = 3$ for which the equilibrium pH was 4.7, i.e., the pI of BSA, and the adsorption was then decreased up to nil with the rise of pH. This was elucidated by the fact that the higher acidity provided the higher degree of protonation of the active centers of both PSLgHap and BSA resulting in the electrostatic repulsion hindering the adsorption, this effect decreased with increasing pH and reached a minimal where the net

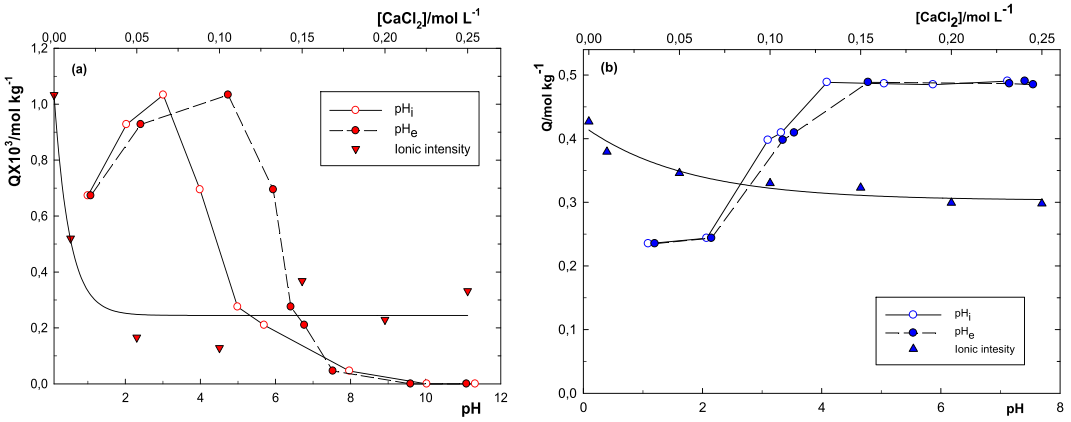

Fig. 7. The effect of pH and ionic strength on BSA (a) and Th^{4+} (b) adsorption ($[BSA]_i$ or $[Th^{4+}]_i$ = 1000 mg L^{-1}, D = 0.1 g PSLgHap/10 mL, T = 298 K) (The ionic strength studies were performed at pH = 3 for BSA and at pH = 4 for Th^{4+}).

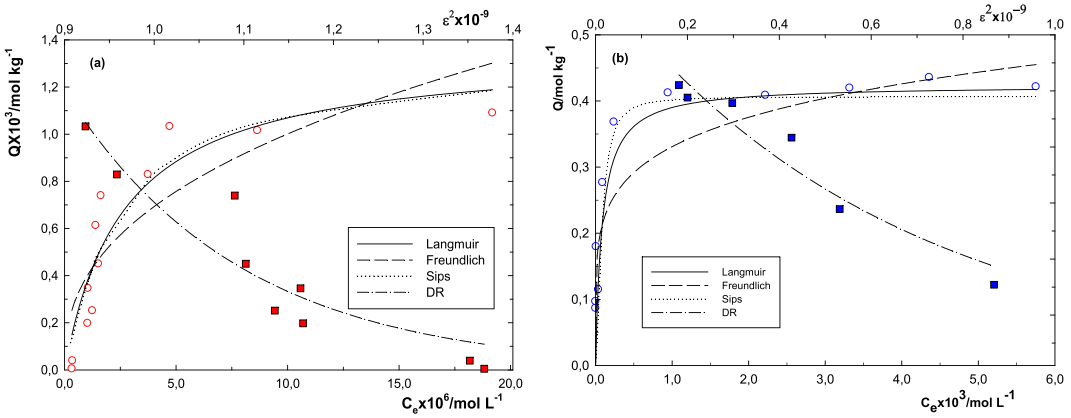

Fig. 8. Compatibility of experimentally obtained BSA (a) and Th^{4+} (b) adsorption to Langmuir, Freundlich, Sips (Q vs C_e), and DR (Q vs ε^2) models ($[BSA]_i$ or $[Th^{4+}]_i$ = 25–2000 mg L^{-1}, D = 0.1 g PSLgHap/10 mL, T = 298 K).

Table 6
Langmuir, Freundlich, Sips, and DR parameters for adsorption of BSA and Th^{4+} onto PSLgHap.

Langmuir	BSA	Th^{4+}	Sips	BSA	Th^{4+}
X_L/mol kg^{-1}	1.35(5.4)[a,b] x10^{-3}	0.42 (1.68)[a,b]	X_S	1.26 × 10^{-3}	0.40
K_L/Lmol^{-1}	376,800	11,600	β_s	1.17	1.75
R^2	0.872	0.940	R^2	0.892	0.944
Freundlich			DR		
X_F	0.10	1.16	X_{DR}	0.12	0.58
β	0.40	0.18	K_{DR}x10^9	5.10	1.56
R^2	0.738	0.880	E_{DR}/kJ mol-1	9.9	17.9
			R^2	0.877	0.933

[a] The extended adsorption value with reference to Lignin-Hap content in PSLgHap (as a mass ratio of 1/4) because the inert feature of PAAm for Th^{4+} and BSA adsorption [32].

[b] Corresponding quantities were 89.7 (359) mg g^{-1} for BSA and 97.4 (390) mg g^{-1} for Th^{4+}.

surface charge of BSA was zero (pI = 4.7) at which maximum adsorption was observed. At pH up to pH = 7.5, the positively charged available on the PSLgHap surface adsorbed BSA under the influence of electrostatic attraction for the negatively charged BSA at pH > pI. This effect became repulsive at pH > PZC since both PSLgHap and BSA were negatively charged such that the magnitude of adsorption eventually reached nil at pH > 7.5. As speculated by Wisniewska et al. [61], the maximum adsorption at pI of BSA was attributed to the formation of BSA in a closely packed conformation at the pI by the influence of mutual intramolecular electrostatic attraction of opposite charges that inactivated the adsorbent–adsorbate electrostatic repulsion. From Fig. 7.a, it was also obvious that the ionic strength of the adsorption medium significantly reduced the adsorption even at the lowest $CaCl_2$ concentration; the adsorption lowered to 30% of its initial value. This should be attributed to the involvement of Ca^{2+} ions predominantly acting as the binding agents for BSA and/or as the competing ions with BSA, both were obstructive for the adsorption. The former is of the metal-protein binding processes in biochemistry [62].

The variation in adsorption of $Th^{4+}$by pH was significant at initial; the amount adsorbed (0.48 mol kg^{-1}) at pH = 4 was two folded of its occurrence at pH = 2. Then, the changes in amounts with pH standstill (Fig. 7b). This should be considered as evidence for the adsorption mechanism was proton exchange and/or complex formation via electrostatic interactions; the probability of Th^{4+} adsorption increased with the increasing number of negatively charged sites of PSLgHap by rising pH. By considering the most dominant Th species in solutions at pH = 1–5 (Th^{4+} and $ThOH^{3+}$) together with the surface charge, the adsorption mechanism should be as follows [47,63,64];

$$4(\equiv SOH) + Th^{4+} \leftrightarrow (\equiv SO)_4Th + 4H^+$$

$$3(\equiv SO^-) + [ThOH]^{3+} \leftrightarrow (\equiv SO^-)_3ThOH$$

Th^{4+}adsorption decreased by the ionic strength of medium ascended such that the 0.42 mol kg^{-1} adsorption from Th^{4+} solution without $CaCl_2$ descended to 0.30 mol kg^{-1} adsorption from that with 0.25 M $CaCl_2$. The initial pH of Th^{4+} solution was about 4 and it was not varied with the $CaCl_2$ additions.

Table 7
BSA sorption capacities of different adsorbents.

Adsorbent	pH	X_L(mg g^{-1})	Reference
Hap powder- Hap disc	6	17.3–67.8	[33]
Hap, Synthetic Hap, and Active Coal	4–7	87.7–57.8, 68.5–55.8, 88.5–30.6	[34]
Al_2O_3 and ZrO_2	5 and 4	81.6 and 26.0	[69]
Hydroxyapatite -Ultrogel Sepracor	5.7–6.7	66.5–17.3	[70]
PAAm and BSA-imprinted PAAm beads	3.7	(1.5–5.6)x10^{-3}	[71]
P(NTBA-co-AAm/MA) hydrogels	5.0	7.2–54.5	[72]
PMA-grafted cellulose/ bentonite	4.5	143.6	[73]
Hap, Asp-, Asn-, Arg-, and Ser-Hap[a]	7.4	6.6, 15.9, 19.3, 28.6, and 17.9	[74]
Spherical-, rod- and fibroid-Hap	7.4	26.5, 28 and 25.7	[75]
PSLgHap	4	89.7 (359)[b]	This study

[a] Amino acid-Hap particles.

[b] The extended adsorption value with reference to SLgHap content of the composite (mass ratio of 1/4).

3.2.3. *The adsorption isotherms*

The compatibility of experimentally obtained isotherm data to Langmuir, Freundlich, Sips, and Dubinin-Radushkevich models by referring to Eqs. (2)–(5) and the parameters derived from the conformities were provided in Fig. 8 and Table 6.

Following the IUPAC physisorption classifications [65], the isotherms were Type-I indicating that PSLgHap had a high affinity to both BSA and Th^{4+} ions. The values of coefficient of variations implied that the Langmuir and the Sips models were best fitted to experimentally obtained adsorption data for both Th^{4+} ($R^2 \geq 0.940$) and BSA ($R^2 \geq 0.872$). The adsorption phenomenon regarding the Langmuir model is that the adsorptive centers available for the adsorbate are energetically equivalent and homogeneously distributed over the composite surface and monolayer adsorption capacity is defined by the amount of species

Table 8
Th^{4+} sorption capacities of different adsorbents.

Adsorbent	X_L (mg g^{-1})	Reference
Hydroxyapatite; PAAm-Hydroxyapatite	185.6 and 127.6	[24]
PAAm-Mt, PAAm-Mt-Phy	76.6; 150.8	[32]
Z, PAAm-Z, PAAm-Z-Phy	16.2; 48.7; 139.2	
ZY; PAAm-ZY; PAAm-ZY-Phy ([a])	171.7; 206.5; 273.8	
PAAm-Ch-Z ([a])	55.7 (167)[b]	[56]
Poly(N,N-diethylacrylamide-*co*-acrylicacid)	25.4	[76]
Iron oxide-impregnated cellulose acetate beads	24.4	[77]
Phosphate-Enhanced Chitin	51	[78]
Ginkgo leaf	104.4	[79]
Amorphous silica	16.2	[80]
Impregnated Sugarcane bagasse	250	[81]
Bio-adsorbent (date palm seed)	42.5	[82]
PSLgHap	97.4 (390)[b]	This study

[a] Mt.: montmorillonite, Z: clinoptilolite, ZY: zeolite Y, Phy: phytic acid, Ch: Chitosan.
[b] The extended adsorption value with reference to Ch-Z and SLgHap contents.

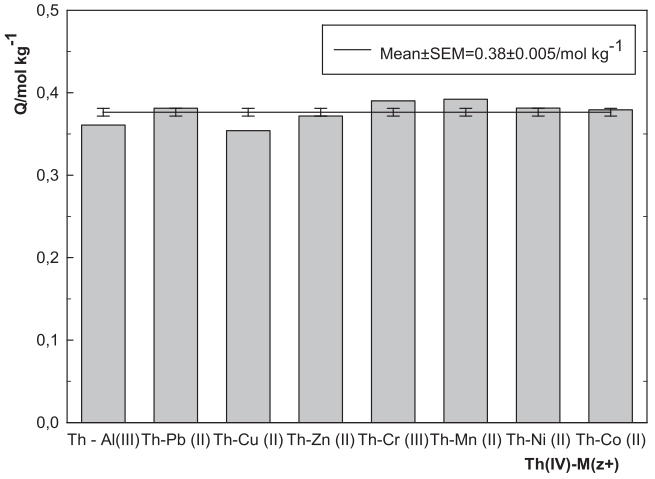

Fig. 9. Adsorption selectivity of PSLgHap for Th^{4+} in the presence of M^{z+} competing cation ($[Th^{4+}]_0 = [M^{z+}]_0 = 4.31 \times 10^{-3}$ mol L^{-1}, D = 0.1 g PSLgHap/10 mL, T = 298 K).

required complete filling of these centers. Conversely to the Langmuir model, the adsorptive sites are heterogeneous and energetically inequivalent proportioned by the Freundlich exponent according to the Freundlich model. Sips model is the united form of two models by an exponent (β_S), which turns into the Langmuir model for $\beta_S = 1$. The higher degree of deviation from '1' is evident for the higher degree of

Table 9
Thermodynamic parameters derived from Van t'Hoff and Gibbs equations for BSA and Th^{4+} adsorption.

BSA			ΔG = ΔH-TΔS / kJ mol^{-1}			
ΔH/kJ mol^{-1}	ΔS/J mol^{-1}	R^2	283 K	293 K	303 K	313 K
31.5	149.0	0.922	−10.7	−12.2	−13.6	−15.1
Th^{4+}						
8.79	85.7	0.909	−15.5	−16.3	−17.2	−18.0

surface heterogeneity, i.e., the modeling shifts to the Freundlich approach. Here, the values of β_S were found to be 1.17 for BSA and 1.75 for Th^{4+}. Based on the previous interpretations [57,66], the adsorption of BSA and predominantly Th^{4+} were harmonious with the Freundlich model at low concentrations (initial part of the isotherm) indicating the filling intensity to the heterogeneously distributed sites. The isotherm was compatible with the Langmuir model at high concentrations to provide monolayer adsorption capacity.

Adsorption free energy derived from the D-R model by Eq. (6) (E_{DR} = 9.9 kJ mol^{-1} for BSA and 17.9 kJ mol^{-1} for Th^{4+} as $E_{DR} < 20$ kJ mol^{-1}) verified that the physicochemical nature of the sorption was Coulomb electrostatic interactions between negatively charged terminals on PSLgHap and BSA or Th^{4+} ions. In brief, the adsorption occurred via the physisorption process including ion exchange and/or complex formation as stated in Section 3.2.2 [67,68].

Langmuir monolayer BSA and Th^{4+} adsorption capacities obtained for PSLgHap were compared with those for various adsorbents extracted from the literature were provided in Tables 7 and 8. As seen, the adsorption capacity of PSLgHap was amongst the ones having considerably high values presented in the table.

Besides its high adsorption capacity, PSLgHap was also selective for Th^{4+} adsorption. For 8 metal ions at di- and tri-valance states selected as competing species (M^{z+}) with Th^{4+} at the equivalent concentration, and as the ions not interfere Th^{4+} determination by colorimetric technique [41]. The mean of Th^{4+} adsorption obtained for 8 ions was 0.38 ± 0.005 mol kg^{-1}. The mean was not significantly different from the amount of adsorption obtained for any of its binary combinations at $p < 0.05$ (Fig. 9).

3.2.4. *The adsorption thermodynamics*

The temperature effect on BSA and Th^{4+} onto PSLgHap were assessed regarding van t'Hoff and Gibbs equations (Eqs. (7)–(9)), and the results were presented in Fig. 10 and Table 9.

The enthalpy and entropy changes were ΔH > 0 and ΔS > 0 for both BSA and Th^{4+} sorption onto PSLgHap. This signifies that the overall process was endothermic and the randomness throughout the adsorption process increased. Gibbs's free enthalpy change was ΔG < 0 for

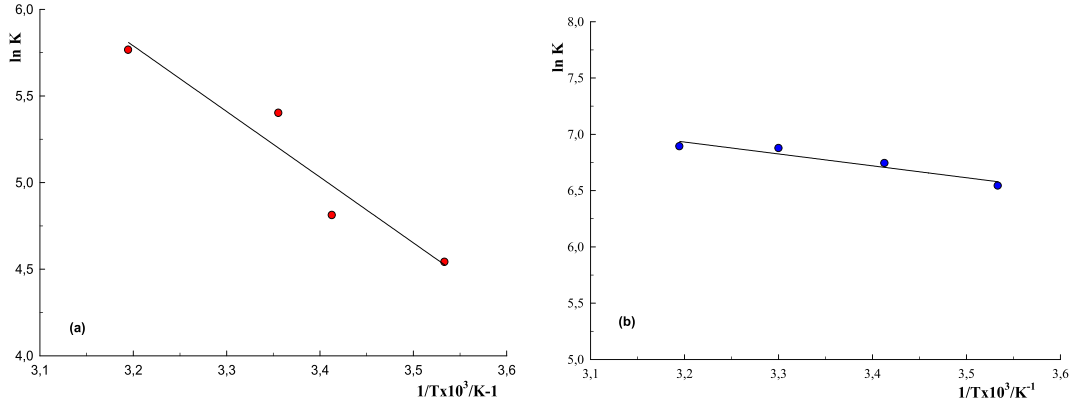

Fig. 10. Temperature dependence of BSA and Th^{4+} adsorption and its compatibility to linearity ($[BSA]_i$ or $[Th^{4+}]_i$ = 1000 mg L^{-1} adsorbent dose = 0.1 g PSLgHap/10 mL, T = 283-313 K).

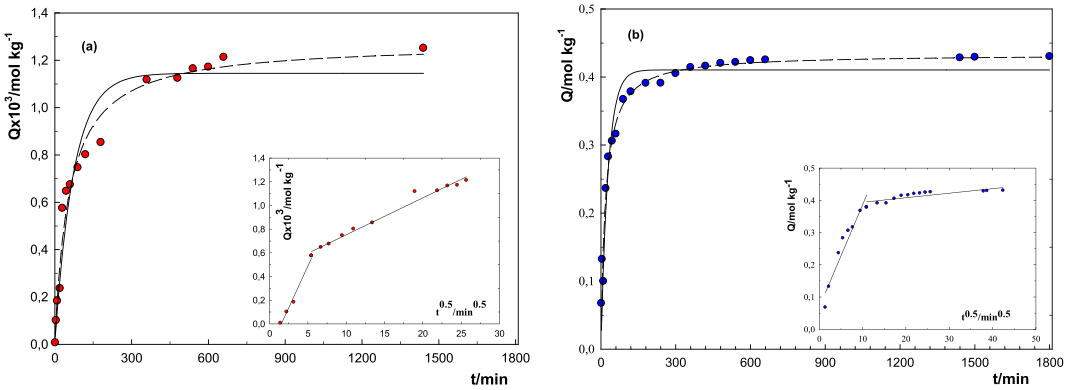

Fig. 11. Compatibility of adsorption kinetics of BSA (a) and Th^{4+} (b) to pseudo first-(—), and second-order (——), and intra-particle diffusion models (inset) ($[BSA]_i$ or $[Th^{4+}]_i$ = 1000 mg L^{-1}, D = 0.5 g PSLgHap/50 mL, T = 298 K).

Table 10
Adsorption kinetics parameters derived from the models considered for BSA and Th^{4+} adsorption onto PSLgHap.

Pseudo first–order	BSA	Th^{4+}	Pseudo second–order	BSA	Th^{4+}
k_1x10^3/min^{-1}	13.6	35	$*k_2/mol^{-1}$ kg min^{-1}	13.4	0.13
$Q_{e1}x10^3/mol$ kg^{-1}	1.15	410	$Q_{e2}x10^3/mol$ kg^{-1}	1.30	430
$Q_{exp}x10^3/mol$ kg^{-1}	1.25	430	$Q_{exp}x10^3/mol$ kg^{-1}	1.25	430
$t_{1/2}$/min	51	20	$t_{1/2}$ /min	58	19
$Hx10^6/mol\ kg^{-1}$ min^{-1}	15.6	143,500	$Hx10^6/mol\ kg^{-1}$ min^{-1}	22.5	2.4 × 10^4
R^2	0.952	0.948	R^2	0.999	0.999
Weber-Morris					
1.Sorption to active centers			2. Intraparticle diffusion		
$k_dx10^3/molkg^{-1}$ $min^{0.5}$	0.14	31.8	$k_ix10^3/molkg^{-1}$ $min^{0.5}$	0.03	1.4
R^2	0.983	0.924	R^2	0.981	0.687
Langmuir Kinetics					
$(\Theta_e)_{exp}$	0.742	1.00			
$(\Theta_e)_{theor}$	0.685	0.875			
k_1/k_2	0.939	0.290			
$(\Theta_e)_{theor}$ - k_1/k_2	−0.254	0.585			

both species indicating that the adsorption process was spontaneous by entropy controlled ($T\Delta S > \Delta H$).

The changes seem to be contrary to the adsorption phenomenon; the expected entropy and enthalpy changes should be negative because the adsorbed molecules represent the transitions of regular and energetically stable states in comparison to its situations in solution. However, it should be stated that the determination of entropy and enthalpy changes special to the adsorbate-adsorbent system in a solution is almost impossible due to the involvement of multi coactions out of the system alone. The values discussed here ultimately represent the changes in thermodynamic magnitudes throughout the whole process in the adsorption environment [83].

3.2.5. The adsorption kinetics

Compatibility of experimentally obtained time-dependent adsorption data to pseudo first- and second-order rates, and intra-particle diffusion models were delineated in Fig. 11. The parameters calculated from the compatibility equations by referring to Eqs. (10)–(12) were tabulated in Table 10.

As seen from the table, the adsorption kinetics of both BSA and Th^{4+} obeyed pseudo second-order model with highly significant coefficients of variation (R^2 = 0.999) for which the closeness of the adsorbed amounts at equilibrium were obtained from the model (Q_{M2}) and the experiment (Q_{exp}) was evident. This suggested that the adsorption was concentration-dependent for both species of interest, i.e., the rate-controlling step was ion exchange and/or complex formation. This was also consistent with the results extracted from the intraparticle diffusion model. The plot did not provide an intercept at origin characterizing the adsorption process controlled by diffusion. But, the shape was curvature that could be evaluated in two linear parts. The initial part with a steep rise was associated with the initial rapid uptake by the boundary layer impact whereas a plateau-like continuation characterized the intraparticle diffusion taking place after the initial uptake [84]. For the present study, the slope of the initial part (k_{ads}) was significantly higher than that of the second part (k_{idif}) for both BSA and Th^{4+}.

According to Liu and Shen [60], the equation '$d\theta_t/d_t = k_1(\theta_e\text{-}\theta_t) + k_2(\theta_e\text{-}\theta_t)^2$' represents a new transformation of the Langmuir kinetics in which the adsorption rate is the combination of the first-order term '$k_1(\theta_e - \theta_t)$' and the second-order term '$k_2(\theta_e - \theta_t)^2$', i.e., it is a hybrid rate equation with a variable reaction order of 1–2. The authors demonstrated that the equation is reduced to first-order rate equation if k_1/k_2 is greater than θ_e or k_1/k_2 is very close to θ_e, and that is reduced to the second-order equation only if $k_1/k_2 << \theta_e$, it remains as the hybrid rate equation otherwise. The calculated values of k_1/k_2 and θ_e by Eqs. (13) and (14) (Table 9) demonstrated that the adsorption of rate was first-order for BSA ($k_1/k_2 > \theta_e$) whereas it was the hybrid-order for Th^{4+} ($k_1/k_2 < \theta_e$). This is contradictive with the above-discussed results related to the pseudo first- and second-order kinetics, which reminds Liu and Shen's remark that the two equations (Eqs. (10)–(11)) have been commonly employed to interpret sorption data even though their theoretical origins remain unknown.

4. Conclusion

The PSLgHap composite was synthesized with 96% efficiency and the characterization tests confirmed that the PSLgHap composite was composed of PAAm and SLgHap. The water absorption capacity of PSLgHap was 8.3 $g_{H2O}g_{PSLgHap}^{-1}$with a high initial rate of 29.3 $g_{H2O}g_{PSLgHap}^{-1}$ min^{-1}. The results associated with the PSLgHap's adsorptive features demonstrated that the maximal adsorption was at pH_i = 3 for BSA and pH_i = 4 for Th^{4+}, increasing ionic intensity of sorption medium significantly lowered BSA adsorption. The best fit to experimentally obtain isotherms was acquired from the Sips model apart from Langmuir, Freundlich, and Dubinin-Radushkevich models. The enthalpy and entropy changes were positive whilst Gibbs energy was negative by entropy controlled. The adsorption kinetics of both species was well compatible with the pseudo second-order model, whereas it was first-order for BSA and hybrid-order for Th^{4+} concerning the Langmuir model. Langmuir parameters signified the high affinity of both BSA and Th^{4+} to PSLgHap for which the monolayer sorption capacities

were as high as 369 and 390 mg g_{SLgHap}^{-1} for BSA and Th^{4+}. This was attributed to the grafting of SL onto Hap increased the adsorption capacity of Hap by the inclusion of chemical groups specific to SL, and/or the synergy effect of PSLgHap's components over the adsorptive attraction. Additionally, the entrapment of SLgHap in the PAAm network also enhanced the adsorption due to the catalytic impact of the adsorptive surface expansion. We anticipate that the inherent adsorptive features of minerals can be enhanced by the integration of lignin derivatives to its body so that the obtained structures become helpful tools for cleaning the wastes.

CRediT authorship contribution statement

Fuat Aslan: Investigation, Validation. **Demet Baybaş:** Investigation, Validation, Writing – original draft. **Ulvi Ulusoy:** Conceptualization, Supervision, Writing – review & editing.

Declaration of competing interest

The authors declare that they have no known competing financial interests or personal relationships that could have appeared to influence the work reported in this paper.

Acknowledgment

The authors would like to acknowledge The Research Fund of Sivas Cumhuriyet University (CÜBAP) for the financial support (Project no: F-430).

References

[1] K.Y. Foo, B.H. Hameed, A short review of activated carbon assisted electrosorption process: an overview, current stage, and future prospects, J. Hazard. Mater. 170 (2009) 552–559, https://doi.org/10.1016/j.jhazmat.2009.05.057.
[2] X. Zhang, A. Lu, D. Li, L. Shi, Z. Luo, C. Peng, Simultaneous removal of methylene blue and Pb2+ from aqueous solution by adsorption on facile modified lignosulfonate, Environ. Technol. 41 (13) (2020) 1677–1690, https://doi.org/10.1080/09593330.2018.1544666.
[3] R. Ahmad, K. Ansari, Enhanced sequestration of methylene blue and crystal violet dye onto green synthesis of pectin modified hybrid (Pect/AILP-Kal) nanocomposite, Process Biochem. 111 (2021) 132–143, https://doi.org/10.1016/j.procbio.2021.10.009.
[4] Q. Yao, J. Xie, J. Liu, H. Kang, Y. Liu, Adsorption of lead ions using a modified lignin hydrogel, J. Polym. Res. 2 (2014) 465, https://doi.org/10.1007/s10965-014-0465-9.
[5] A. Grossman, W. Vermerris, Lignin-based polymers and nanomaterials, Curr. Opin. Biotechnol. 56 (2019) 112–120, https://doi.org/10.1016/j.copbio.2018.10.009.
[6] M. Culebras, A. Barrett, M. Pishnamazi, G.M. Walker, M.N. Collins, Wood-derived hydrogels as a platform for drug-release systems, ACS Sustain. Chem. Eng. 9 (2021) 2515–2522, https://doi.org/10.1021/acssuschemeng.0c08022.
[7] A. Beaucamp, M. Culebras, M.N. Collins, Sustainable mesoporous carbon nanostructures derived from lignin for early detection of glucose, Green Chem. 23 (2021) 5696–5705, https://doi.org/10.1039/D1GC02062E.
[8] Y. Ge, Z. Li, Application of lignin and its derivatives in adsorption of heavy metal ions in water: a review, ACS Sustain. Chem. Eng. 6 (2018) 7181–7192, https://doi.org/10.1021/acssuschemeng.8b01345.
[9] Y. Meng, J. Lua, Y. Cheng, Q. Li, H. Wang, Lignin-based hydrogels: a review of preparation, properties, and application, Int. J. Biol. Macromol. 135 (2019) 1006–1019, https://doi.org/10.1016/j.ijbiomac.2019.05.198.
[10] M. Österberg, M.H. Sipponen, B.D. Mattos, O.J. Rojas, Spherical lignin particles: a review on their sustainability and applications, Green Chem. 22 (2020) 2712, https://doi.org/10.1039/D0GC00096E.
[11] D. Rico-García, L. Ruiz-Rubio, L. Pérez-Alvarez, S.L. Hernández-Olmos, G. L. Guerrero-Ramírez, J.L. Vilas-Vilela, Lignin-based hydrogels: synthesis and applications, Polymers 12 (2020) 81, https://doi.org/10.3390/polym12010081.
[12] Y. Wang, Z. Li, D. Yang, X. Qiu, Y. Xie, X. Zhang, Microwave-mediated fabrication of silver nanoparticles incorporated lignin-based composites with enhanced antibacterial activity via electrostatic capture effect, J. Colloid Interface Sci. 583 (2021) 80–88, https://doi.org/10.1016/j.jcis.2020.09.027.
[13] N. Supanchaiyamat K. Jetsrisuparb J.T.N. Knijnenburg D.C.W. Tsang A.J. Hunt, Lignin materials for adsorption: current trend, perspectives, and opportunities, Bioresour. Technol. 272 (209) 570–581. doi:10.1016/j.biortech.2018.09.139.
[14] A. Mirza, R. Ahmad, An efficient sequestration of toxic crystal violet dye from aqueous solution by Alginate/Pectin nanocomposite: a novel and ecofriendly adsorbent, Groundw. Sustain. Dev. 11 (2020), 100373, https://doi.org/10.1016/j.gsd.2020.100373.
[15] T. Kanno, T. Sendai, K. Tada, J.I. Horiuchi, T. Akazawa, Adsorption properties of acidic and basic proteins on the surface of carbonate-containing hydroxyapatite, Phosphorus Res. Bull. 21 (2007) 25–30, https://doi.org/10.3363/prb.21.25.
[16] K. Kandori, S. Mizumoto, S. Toshima, M. Fukusumi, Y. Morisada, Effects of heat treatment of calcium hydroxyapatite particles on the protein adsorption behavior, J. Phys. Chem. B 113 (2009) 11016–11022, https://doi.org/10.1021/jp904481z.
[17] K. Wang, C. Zhou, Y. Hong, X. Zhang, A review of protein adsorption on bioceramics, Interface Focus 2 (2012) 259–277, https://doi.org/10.1098/rsfs.2012.0012.
[18] T. Nagasaki, F. Nagata, M. Sakurai, K. Kato, Effects of pore distribution of hydroxyapatite particles on their protein adsorption behavior, J. Asian Ceram. Soc. 5 (2017) 88–93, https://doi.org/10.1016/j.jascer.2017.01.005.
[19] M. Ibrahim, M. Labaki, J.M. Giraudon, J.-F. Lamonier, Hydroxyapatite, a multifunctional material for air, water and soil pollution control: a review, J. Hazard. Mater. 383 (5) (2020) 121–139, https://doi.org/10.1016/j.jhazmat.2019.121139.
[20] S. Choi, Y. Jeong, The removal of heavy metals in aqueous solution by hydroxyapatite/cellulose composite, Fibers Polym. 9 (2008) 267–270.
[21] S.H. Jang, G.M. Min, Y.G. Jeong, W.S. Lyoo, S.C. Lee, Removal of lead ions in aqueous solution by hydroxyapatite/polyurethane composite foams, J. Hazard. Mater. 152 (3) (2008) 1285–1292, https://doi.org/10.1016/j.jhazmat.2007.08.003.
[22] X. Wang, J.H. Kim, B.G. Min, Column study of cadmium adsorption onto poly(vinyl alcohol)/hydroxyapatite composite cryogel, Fibers Polym. 9 (2008) 263–266.
[23] S.H. Jang, Y.G. Jeong, B.G. Min, W.S. Lyoo, S.C. Lee, Preparation and lead ion removal property of hydroxyapatite/polyacrylamide composite hydrogels, J. Hazard. Mater. 159 (2008) 294–299, https://doi.org/10.1016/j.jhazmat.2008.02.018.
[24] D. Baybaş, U. Ulusoy, Polyacrylamide–hydroxyapatite composite: preparation, characterization and adsorptive features for uranium and thorium, J. Solid State Chem. 194 (2012) 1–8, https://doi.org/10.1016/j.jssc.2012.07.039.
[25] Z. Li, W. Mi, H. Wang, Y. Su, C. He, Nano-hydroxyapatite/polyacrylamide composite hydrogels with high mechanical strengths and cell adhesion properties, Colloids Surf. B: Biointerfaces 123 (2014) 959–964, https://doi.org/10.1016/j.colsurfb.2014.10.050.
[26] J.J. Meister, D.R. Patil, H. Channell, Properties and applications of lignin–acrylamide graft copolymer, J. Appl. Polym. Sci. 29 (1984) 3457–3477, https://doi.org/10.1002/app.1984.070291122.
[27] J.E. Peñaranda, M.A. Sabino, Effect of the presence of lignin or peat in IPN hydrogels on the sorption of heavy metals, Polym. Bull. 65 (2010) 495–508, https://doi.org/10.1007/s00289-010-0264-3.
[28] C. Mai, O. Milstein, A. Hüttermann, Chemoenzymatical grafting of acrylamide onto lignin, J. Biotechnol. 79 (2000) 173–183, https://doi.org/10.1016/S0168-1656(00)00230-3.
[29] Y. Chen, K. Zheng, L. Liu, Y. Zhang, Y. Liu, C. Wang, F. Chu, Highly mechanical properties nanocomposite hydrogels with biorenewable lignin nanoparticles, Int. J. Biol. Macromol. 128 (2019) 414–420, https://doi.org/10.1016/j.ijbiomac.2019.01.099.
[30] A. Hasan, P. Fatehi, Self-assembly of kraft lignin-acrylamide polymers, Colloids Surf. A Physicochem. Eng. Asp. 572 (2019) 230–236, https://doi.org/10.1016/j.colsurfa.2019.04.002.
[31] S. Erakovic, A. Jankovic, I.Z. Matic, Z.D. Juranic, M. Vukasinovic-Sekulic, T. Stevanovic, V. Miskovic-Stankovic, Investigation of silver impact on hydroxyapatite/lignin coatings electrodeposited on titanium, Mater. Chem. Phys. 142 (2013) 521–530, https://doi.org/10.1016/j.matchemphys.2013.07.047.
[32] D. Baybaş, U. Ulusoy, The use of polyacrylamide-aluminosilicate composites for thorium adsorption, Appl. Clay Sci. 51 (2011) 138–146, https://doi.org/10.1016/j.clay.2010.11.020.
[33] E. Mavropoulos, A.M. Costa, L.T. Costa, C.A. Achete, A. Melloa, J.M. Granjeiroe, A. M. Rossi, Adsorption and bioactivity studies of albumin onto hydroxyapatite surface, Colloids Surf. B: Biointerfaces 83 (2011) 1–9, https://doi.org/10.1016/j.colsurfb.2010.10.025.
[34] M.R.R. Alves, A.D.G. Zuñiga, R.C.S. Sousa, C.Z. Scolforo, The process of separating bovine serum albumin using hydroxyapatite and active babassu coal (Orbignya martiana), Sci. World J. 2808241 (2016) 9, https://doi.org/10.1155/2016/2808241.
[35] T. Kopac, Protein corona, understanding the nanoparticle–protein interactions and future perspectives: a critical review, Int. J. Biol. Macromol. 169 (2021) 290–301, https://doi.org/10.1016/j.ijbiomac.2020.12.108.
[36] N.A.S. Mohd Pu'ad, P. Koshy, H.Z. Abdullah, M.I. Idris, T.C. Lee, Syntheses of hydroxyapatite from natural sources, Heliyon. 5 (2019), e01588, https://doi.org/10.1016/j.heliyon.2019.e01588.
[37] E. Mavropoulos, C.C.N. Rocha, C.J. Moreira, C.L. Bertolino, M.A. Rossi, Pb2+, Cu2 + and Cd2+ ions uptake by brazilian phosphate rocks, J. Braz. Chem. Soc. 16 (2005) 62–68, https://doi.org/10.1590/S0103-50532005000100010.
[38] E.S. Dragan, M.V. Dinu, D. Timpu, Preparation and characterization of novel composites based on chitosan and clinoptilolite with enhanced adsorption properties for Cu2+, Bioresour. Technol. 101 (2010) 812–817, https://doi.org/10.1016/j.biortech.2009.08.077.
[39] H.D. Chapman, Cation-exchange capacity, in: A.G. Norman (Ed.), Methods of Soil Analysis-Part 2. Chemical and Microbiological Properties. Agronomy Monograph 9.2, American Society of Agronomy, Soil Science Society of America. Inc, 1965, pp. 891–901, https://doi.org/10.2134/agronmonogr9.2.c6.
[40] M. Mullet, P. Fievet, A. Szymczyk, A. Foissy, J.-C. Reggiani, J. Pagetti, A simple and accurate determination of the point of zero charge of seramic membranes,

Desalination 121 (1999) 41–48, https://doi.org/10.1016/S0011-9164(99)00006-5.
[41] M. Khan, A. Ali, N. Khan, Spectrophotometric determination of thorium with disodium salt of arsenazo-III in perchloric acid, J. Radioanal. Nucl. Chem. 250 (2) (2001) 353–357, https://doi.org/10.1023/A:1017968217578.
[42] F. He, Bradford protein assay, Bio- 101 (2011), e45, https://doi.org/10.21769/BioProtoc.45.
[43] R.T. Yang, Adsorbents: Fundamentals and Applications, first ed., John Wıley & Sons, Inc, Canada, 2003.
[44] H. Gheisari, E. Karamian, M. Abdellahi, A novel hydroxyapatite–hardystonite nano composite ceramic, Ceram. Int. 41 (2015) 5967–5975, https://doi.org/10.1016/J.CERAMINT.2015.01.033.
[45] V. Nair, A. Panigrahy, R. Vinu, Development of novel chitosan–lignin composites for adsorption of dyes and metal ions from wastewater, Chem. Eng. J. 254 (2014) 491–502, https://doi.org/10.1016/j.cej.2014.05.045.
[46] T. Rashid, C.F. Kait, T. Murugesan, A "Fourier transformed infrared" compound study of lignin recovered from a formic acid process, Procedia Eng. 148 (2016) 1312–1319, https://doi.org/10.1016/j.proeng.2016.06.547.
[47] D. Baybaş, U. Ulusoy, Polyacrylamide-clinoptilolite/Y-zeolite composites: characterization and adsorptive features for terbium, J. Hazard. Mater. 187 (2011) 241–249, https://doi.org/10.1016/j.jhazmat.2011.01.014.
[48] A.M. Dumitrescu, G. Lisa, A.R. Iordan, F. Tudorache, I. Petrila, A.I. Borhan, M. N. Palamaru, C. Mihailescu, L. Leontie, C. Munteanu, Ni ferrite highly organized as humidity sensors, Mater. Chem. Phys. 156 (2015) 170–179, https://doi.org/10.1016/j.matchemphys.2015.02.044.
[49] Y.X. Pang, X. Bao, Influence of temperature, ripening time and calcination on the morphology and crystallinity of hydroxyapatite nanoparticles, J. Eur. Ceram. Soc. 23 (2003) 1697–1704, https://doi.org/10.1016/S0955-2219(02)00413-2.
[50] V.M. Rusu, C.-H. Ng, M. Wilke, B. Tiersch, P. Fratzl, M.G. Peter, Size-controlled hydroxyapatite nanoparticles as self-organized organic–inorganic composite materials, Biomaterials 26 (2005) 5414–5426, https://doi.org/10.1016/j.biomaterials.2005.01.051.
[51] K. Tõnsuaadu, K.A. Gross, L. Pluduma, M. Veiderma, A review on the thermal stability of calcium apatites, J. Therm. Anal. Calorim. 110 (2012) 647–659, https://doi.org/10.1007/s10973-011-1877-y.
[52] A.G. Khudoshin, V.V. Lunin, V. Bogdan, Conversion of veratrole and sodium lignosulfonate in the sub- and supercritical water, Russ. J. Phys. Chem. 5 (2011) 1069–1075, https://doi.org/10.1134/S1990793111070037.
[53] H. Yang, R. Yan, H. Chen, D.H. Lee, C. Zheng, Characteristics of hemicellulose, cellulose and lignin pyrolysis, Fuel 86 (2007) 1781–1788, https://doi.org/10.1016/j.fuel.2006.12.013.
[54] W. Wang, A. Wang, Synthesis and swelling properties of guar gum-gpoly(sodium acrylate)/Na-montmorillonite superabsorbent nanocomposite, J. Compos. Mater. 43 (2009) 2805–2819, https://doi.org/10.1177/0021998309345319.
[55] X.-F. Sun, Z. Jing, G. Wang, Preparation and swelling behaviors of porous hemicellulose-g-polyacrylamide hydrogels, J. Appl. Polym. Sci. 128 (2013) 1861–1870, https://doi.org/10.1002/app.38240.
[56] O. Eninanç, U. Ulusoy, Preparation and characterization of chitosan-zeolite composite@polyacrylamide: adsorptive features for thorium, in: N.R. Blevins (Ed.), An Introduction to Aluminosilicates, Nova Science Publishers, Inc, New York, 2020, pp. 361–388.
[57] K.Y. Foo, B.H. Hameed, Insights into the modeling of adsorption isotherm systems, Chem. Eng. J. 156 (2010) 2–10, https://doi.org/10.1016/j.cej.2009.09.013.
[58] Y.S. Ho, G.A. McKay, Comparison of chemisorption kinetic models applied to pollutant removal on various sorbents, Process. Saf. Environ. Prot. 76 (1998) 332–340, https://doi.org/10.1205/095758298529696.
[59] S. Basha, Z.V.P. Murthy, Kinetic and equilibrium models for biosorption of cr (VI) on chemically modified seaweed, Cystoseira indica, Process Biochem. 42 (2007) 1521–1529, https://doi.org/10.1016/j.procbio.2007.08.004.
[60] Y. Liu, L. Shen, From Langmuir kinetics to first- and second-order rate equations for adsorption, Langmuir 24 (2008) 11625–11630, https://doi.org/10.1021/la801839b.
[61] M. Wisniewska, K. Szewczuk-Karpisz, D. Sternik, Adsorption and thermal properties of the bovine serum albumin–silicon dioxide system, J. Therm. Anal. Calorim. 120 (2015) 1355–1364, https://doi.org/10.1007/s10973-014-4300-7.
[62] A. Besarab, A. Deguzman, J.W. Swanson, Effect of albumin and free calcium concentrations on calcium binding in vitro, J. Clin. Pathol. 34 (1981) 1361–1367, https://doi.org/10.1136/jcp.34.12.1361.
[63] C. Moulin, B. Amekraza, S. Hubert, V. Moulin, Study of thorium hydrolsis species by electrospray-ionization mass spectrometry, Anal. Chim. Acta 441 (2001) 269–279, https://doi.org/10.1016/S0003-2670(01)01084-4.
[64] C. Ekberg, Y. Albinsson, M.J. Comarmond, P.L. Brown, Studies on the complexation behavior thorium (IV). 1. Hydrolysis equilibria, J. Solut. Chem. 29 (2000) 63–86.
[65] K.S.W. Sing, Reporting physisorption data for gas/solid systems with special reference to the determination of surface area and porosity, Pure Appl. Chem. 54 (11) (1982) 2201–2218.
[66] A. Günay, E. Arslankaya, İ. Tosun, Lead removal from aqueous solution by natural and pretreated clinoptilolite: adsorption equilibrium and kinetics, J. Hazard. Mater. 146 (2007) 362–371, https://doi.org/10.1016/j.jhazmat.2006.12.034.
[67] P. Atkins, J. Paula, in: Physical Chemistry, 8th ed., Oxford University Press, GB, 2006, pp. 916–917.
[68] A.U. Itodo, H.U. Itodo, Sorption energies estimation using dubinin-radushkevich and temkin adsorption isotherms, Life Sci. J. 7 (2010) 31–39.
[69] K. Bozgeyik, T. Kopac, Adsorption of bovine serum albumin onto metal oxides: adsorption equilibrium and kinetics onto alumina and zirconia, Int. J. Chem. React. 8 (1) (2010), https://doi.org/10.2202/1542-6580.2336.
[70] C. Fargues, M. Bailly, G. Grevillot, Adsorption of BSA and hemoglobin on hydroxyapatite support: equilibria and multicomponent dynamic adsorption, Adsorption 4 (1998) 5–16, https://doi.org/10.1023/A:1008822918494.
[71] X. Pang, G. Cheng, S. Lu, E. Tang, Synthesis of polyacrylamide gel beads with electrostatic functional groups for the molecular imprinting of bovine serum albümin, Anal. Bioanal. Chem. 384 (2006) 225–230, https://doi.org/10.1007/s00216-005-0147-x.
[72] G. Demirel, Adsorption of bovine serum albumin onto poly(N-t-butylacrylamide-co-acrylamide/maleic acid), J. Polym. Res. 14 (2007) 23–30, https://doi.org/10.1007/s10965-006-9076-4.
[73] T.S. Anirudhan, A.R. Tharun, S.R. Rejeen, Investigation on poly(methacrylic acid)-grafted cellulose/bentonite superabsorbent composite: synthesis, characterization, and adsorption characteristics of bovine serum albumin, Ind. Eng. Chem. Res. 50 (2011) 1866–1874, https://doi.org/10.1021/ie101918m.
[74] W.-H. Lee, C.-Y. Loo, K.L. Van, A.V. Zavgorodniy, R. Rohanizadeh, Modulating protein adsorption onto hydroxyapatite particles using different amino acid treatments, J. R. Soc. Interface 9 (2012) 918–927, https://doi.org/10.1098/rsif.2011.0586.
[75] S.K. Swain, D. Sarkar, Study of BSA protein adsorption/release on hydroxyapatite nanoparticles, Appl. Surf. Sci. 286 (2013) 99–103, https://doi.org/10.1016/j.apsusc.2013.09.027.
[76] H. Peizhuo, L. Tonghuan, Z. Gen, D. Xiaojiang, W. Wangsuo, Adsorption of Th4+ from aqueous solution onto poly(N, ndiethylacrylamide-co-acrylic acid) microgels, J. Radioanal. Nucl. Chem. 301 (2014) 65–73, https://doi.org/10.1007/s10967-014-3154-6.
[77] P.D. Bhalara, D. Punetha, K. Balasubramanian, Kinetic and isotherm analysis for selective thorium(IV) retrieval from aqueous environment using eco-friendly cellulose composite, Int. J. Environ. Sci. Technol. 12 (2015) 3095–3106, https://doi.org/10.1007/s13762-014-0682-0.
[78] M.A. Gado, A.M.A. Morsy, Thorium adsorption from waste effluents by phosphate-enhanced chitin radiochemistry, Radiochemistry 59 (2016) 500–506, https://doi.org/10.1134/S1066362217050101.
[79] Y. Huang, Y. Hu, L. Chen, T. Yang, H. Huang, R. Shi, P. Lu, C. Zhong, Selective biosorption of thorium (IV) from aqueous solutions by ginkgo leaf, PLoS One 13 (3) (2018), e0193659, https://doi.org/10.1371/journal.pone.0193659.
[80] Ü.H. Kaynar, I. Şabikoğlu, Adsorption of thorium (IV) by amorphous silica; response surface modeling and optimization, J. Radioanal. Nucl. Chem. 318 (2018) 823 834, https://doi.org/10.1007/s10967-018-6044-5.
[81] A.R. Bakry, Synthesis of quinoline/phenanthroline impregnated sugarcane bagasse for recovering Uranium(VI) and Thorium(IV) from their solutions, Z. Anorg. Allg. Chem. 646 (2020) 377–389, https://doi.org/10.1002/zaac.202000114.
[82] A. Sayed, M. Abdelmottaleb, M.F. Cheira, G. Abdel-Aziz, H. Gomaa, T.F. Hassanein, Date seed as an efficient, eco-friendly, and cost-effective bio-adsorbent for removal of thorium ions from acidic solutions, Aswan Univ. J. Environ. Stud. 1 (1) (2020) 106–124, https://doi.org/10.21608/AUJES.2020.124579.
[83] D. Baybaş, U. Ulusoy, Adsorptive features of polyacrylamide aluminosilicate composites for methylene blue, Turk. J. Chem. 40 (2016) 147–162, https://doi.org/10.3906/kim-1504-32.
[84] Y. Khambhaty, K. Mody, S. Basha, B. Jha, Kinetics, equilibrium and thermodynamic studies on biosorption of hexavalent chromium by dead fungal biomass of marine aspergillus Niger, Chem. Eng. J. 145 (2009) 489–495, https://doi.org/10.1016/j.cej.2008.05.002.